Theory of multiresonant metamaterials for A_0 Lamb waves

Earl G. Williams*
Naval Research Laboratory, Code 7106, Acoustics Division, 4555 Overlook Avenue, Washington, DC 20375, USA

Philippe Roux and Matthieu Rupin
Institut des Sciences de la Terre, UMR 5275, Universit Joseph Fourier, 38000 Grenoble, France

W. A. Kuperman
Scripps Institution of Oceanography, University of California San Diego, 9500 Gilman Drive, La Jolla, California 92093-0238, USA
(Received 22 January 2015; revised manuscript received 3 March 2015; published 23 March 2015)

We develop an analytical wave approach to describe the physics properties of multiresonant metamaterials for Lamb waves propagating in plates. The metamaterial that we characterize consists of a 10 by 10 uniform, periodic array of long rods attached to the surface of the plate that forms the substrate in which antisymmetric A_0 Lamb waves are excited. We show that the A_0 Lamb wave propagation through the metamaterial can be accurately modeled using a simplified theory that replaces the two-dimensional array with a one-dimensional beam with a linear array of 10 rods. The wave propagation problem is solved rigorously for this one-dimensional system using the scattering matrix for a single rod. The exact eigenvalues of the system are approximated in a long wavelength expansion to determine a simple expression for the effective wave number and dispersion of the metamaterial. The modeled dispersion is compared with an experimental measurement of the dispersion inside the metamaterial with excellent agreement. The multiresonant rods, restricted to longitudinal vibration consistent with A_0 Lamb waves excited in the plate, produce two wide stop bands in the frequency domain from 0 to 10 kHz where the stop or passband boundaries align with the minima and maxima of the rod's impedance. We show that a negative effective density is obtained in the stop band. With the simple yet highly accurate relations given in this paper we have a tool to develop more complex metamaterials with rods and plates of different properties.

DOI: 10.1103/PhysRevB.91.104307 PACS number(s): 43.20.+g, 43.40.+s, 46.40.Cd, 46.40.Ff

I. INTRODUCTION

Manmade composite materials have been the subject of many investigations in the wave physics community over the last decade, as they show wave field characteristics that cannot be obtained with natural materials. Metamaterials therefore provide an opportunity to control and manipulate waves at different wavelength scales. In general, the wave propagation properties of these media find their roots in two distinct origins: first, the ordered or disordered spatial organization of their components; second, the resonant or nonresonant nature of their unitary element. When waves propagate in a complex medium with structural order, they can undertake single or multiple scattering, which leads to frequency bands of permitted and forbidden propagation, also called band gaps. These forbidden frequency bands are analogous to electronic band gaps in natural crystals (Kittel) [1]. These materials have a typical spatial scale comparable to the average wavelength of the wave under investigation. They are termed photonic crystals in electromagnetics and phononic crystals in acoustics, and they constitute powerful tools to shape the wave field in various manners (Yablonovitch [2], Joannopoulos [3], Deymier) [4].

Other types of composite materials are made of a collection of unitary resonant components (subwavelength resonators) from which they extract their dispersive properties at the macroscopic scale (Liu [5], Pendry [6], Engheta and Ziolkowski) [7]. A key parameter of these so-called locally resonant metamaterials lies in the arrangement of many subwavelength resonators within a wavelength (Liu [8], Wu [9], Lemoult) [10]. Thus, the proximity of subwavelength resonators permits the coupling between a large set of individual resonators. In this case the metamaterial physics can be interpreted through interferences between the incident field and the scattered waves generated by each resonant unit. At the macroscopic scale, local resonances lead to the hybridization phenomenon that deeply modify the dispersion curve in the host medium (Lemoult) [11]. Contrary to photonic or phononic crystals, which exhibit band gaps due to the Bragg diffraction effect, the spatial organization of locally resonant metamaterial is no longer relevant, which means that band gaps can be observed independently of its ordered or disordered nature (Kaina) [12].

The width and efficiency of band gaps in locally resonant metamaterials depend upon both the spatial density of the resonators and the quality factor of the resonances. In the limit of small resonators compared to the wavelength, the smaller the resonator, the higher its quality factor. This justifies why locally resonant metamaterials classically support band gaps limited to narrow bandwidths. To overcome this fundamental limitation, metamaterials can be created with resonator units that are small in two dimensions that support wave propagation, but elongated in the third one, where each resonator can expand. Such a uni-axial metamaterial was created with a so-called wire medium in electromagnetism, which has been used to control and/or focus waves below the diffraction limit (Belov [13], Lerosey [14], Lemoult) [15]. In acoustics, a collection of narrow, but long, pipes was recently used to form a super lens (Zhu) [16]. This approach is also perfectly suited to 2D plate waves that interact with

*Corresponding author: earl.williams@nrl.navy.mil

a collection of vertical rods, as will be shown in the present paper.

The goal of the paper is to propose an analytical wave propagation matrix approach to describe the physics properties of multiresonant metamaterials for Lamb waves propagating in plates with small diameter, elongated rods perpendicular to the plates. Experimentally, we find that vibration coupling between these rods and the plate are between the rods' longitudinal waves and the plate's transverse, mainly A_0, waves. This driving *point* force on the plate at each location of the rod is tantamount to a single mode coupling so that an effective metamaterial wave number can be derived. Homogenization schemes (see, for example Torrent [17], Wu [9], and Yang [18] and references therein) that identify the individual effective metamaterial parameters such as elastic moduli and density require multimodal scattering within the unit cell and are therefore not employed. The advantage of the proposed methodology is the full prediction of the dispersion curve from which metamaterial physics can be investigated and potential applications can be designed.

The motivation of the theoretical work proposed here was the experimental demonstration of metamaterial physics in Rupin [19]. In this paper, the authors investigated the propagation of elastic waves in a system formed by a set of aluminum rods glued to a thin aluminum plate (1.5 m × 2 m × 6 mm). A collection of 100 long rods (length, 61 cm) was attached perpendicularly to the plate inside a 20 cm × 20 cm square (Fig. 1). These thin rods (diameter, 6 mm) form a set of quasipunctual resonators whose total size is comparable to the average wavelength of the flexural waves in the plate (≈ 0.2 m). It was possible to arrange these rods periodically or

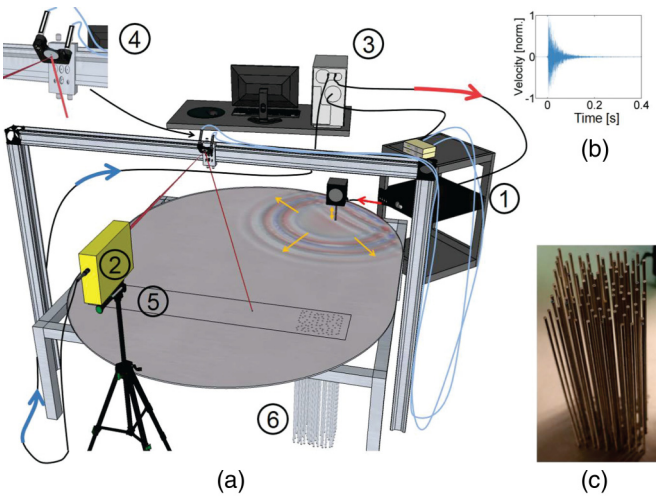

FIG. 1. (Color online) (a) Experimental setup at the laboratory scale. A shaker (1) generates A_0 Lamb waves in an aluminum plate. The wave field is measured with a Doppler velocimeter (2) and a PC-controlled (3) motorized mirror (4) on the rectangular area (5) on the upper side of the plate. The metamaterial (6) is attached below the plate on one side of the recording map. (b) The typical temporal dispersion exceeds 0.2 s, which corresponds to more than 20 round trips inside the plate. (c) The metamaterial is made of 100 vertical aluminium rods that can be arranged in a periodic or random pattern, with an average interrod distance on the order of 2 cm (from Rupin) [19].

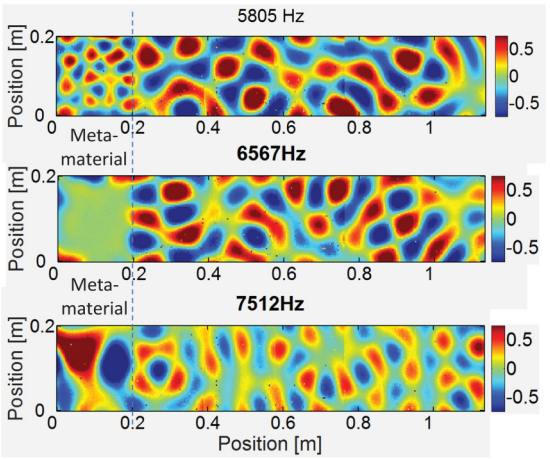

FIG. 2. (Color online) Spatial representation of the normal velocity experimentally measured in the region indicated by the rectangular area on the plate in Fig. 1. The 10 × 10 rod region is on the left between 0 and 0.2 m. Three frequencies are shown: the top is just before a stop band of the metamaterial, the center is a frequency in the stop band, and the lower plot is just above the stop band.

randomly at a subwavelength scale. The combination of these 100 rods glued to the plate provided an original metamaterial at the mesoscopic scale. Due to the strong reverberation at the plate boundaries [Fig. 1(b)], the experiment showed a complex diffuse wave field within the plate that included wide band gaps inside the metamaterial (Fig. 2).

These experimental results confirmed the hybridization phenomenon between the dominant flexural A_0 mode in the plate and the compressional resonances inside the rods and demonstrated the presence of subwavelength and suprawavelength modes within the metamaterial before and after each band gap (Fig. 2). The spatial measurements described in Fig. 1 at three different frequencies show the diversity of results that can be obtained within the metamaterial (the region on the left between 0 and 0.2 m). In particular, one can see clearly that the spatial wavelength is different within and outside the metamaterial.

The main objective of the present paper is to provide an analytical formalism based on the 1D description of the scattered wave field to fully interpret these results. While Rupin *et al.* [19] were able to model the propagation within the metamaterial using numerical simulation (finite elements) on the unit cell with Bloch periodic conditions on its boundary, the goal is here to provide an analytical formalism based on the one-dimensional (1D) description of the scattered wave field to go further in the interpretation of these results.

The paper is structured as follows. We provide the development of the 1D theory in Secs. II and II A, developing the scattering matrix for the rod using the boundary conditions at the rod-beam interface in Sec. II B. The transmission matrix through the rod forest is developed in Sec. II C. An eigenanalysis is presented in Sec. II D, and the eigenvalues are determined and approximated using a kL expansion, detailed in the Appendix. From this the effective wave number of the 1D array is developed along with the attenuation in the stop band. Section III details the comparison to the experiment with a uniform rectangular array of resonators on a large point driven

plate. In Sec. IV we turn to address the observation given in Rupin [19] that in their plate experiment with a 10×10 array of rods, the passband and stop bands developed independent of the arrangement of the rod forest, a random spaced grid behaved the same as one with uniform spacing. We corroborate this observation with a brief mathematical analysis. Finally conclusions are presented.

II. MATHEMATICAL ANALYSIS

Powerful mathematical approaches that deal with a two-dimensional (2D) array of cylinders imbedded in a substrate are readily found in the literature. Torrent [17] provides a general solution to the problem using 2D expansions of the fields in terms of Bessel functions. Gracia-Salgado [20] studied an air substrate imbedded with fluid cylindrical shells using three-dimensional (3D) expansions of the fields in terms of Bessel functions and waveguide modes. Similar 2D expansions with Bessel functions are used by Lagarrigue [21] to study the transmission through a forest of bamboo rods in air. With much more mathematical complexity, Liu [8] and Wu [9] study an elastic substrate with embedded cylinders and spheres (respectively) solving the problem rigorously using expansions in terms of the 2D eigenfunctions for the geometry.

Instead of proceeding along the rather complicated mathematical lines of the above references, we have investigated the success of the prediction of the behavior of our metamaterial [10×10 array of rods shown in Fig. 1(c)] using a simplified mathematical method based on a 1D model. In Fig. 3 the 10×10 rod forest is replaced with a 1D infinite beam (top) with 10 rods, which is again subdivided into a unit cell (bottom) for the purpose of our study. The width of the beam is equal to the spacing between the rods, and the beam is of the same material and thickness as the plate. We include only the A_0 flexural Lamb waves of the beam, since the excitation used in the experiment is an out-of-plane force generator. In-plane extensional vibration (S_0 Lamb wave) is not excited and is omitted in the following analysis.

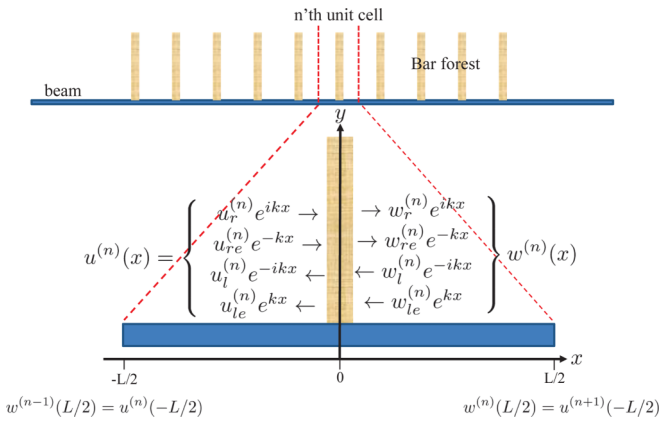

FIG. 3. (Color online) A unit cell consisting of a rod (vertical rectangle) attached to a beam (horizontal rectangle). The waves traveling in the beam on either side of a rod are shown. These waves are the out-of-plane flexural (A_0 mode) vibration. The arrows indicate direction of wave propagation. The superscript is the segment number. The segment is of length L with ends at $x = \pm L/2$, and the rod is attached at $x = 0$.

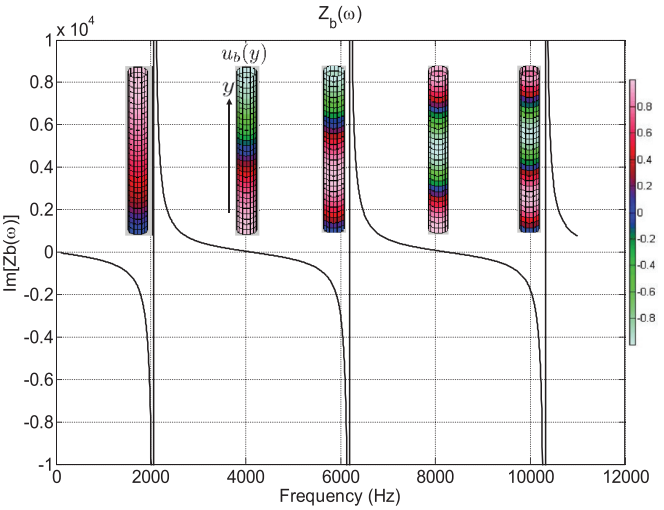

FIG. 4. (Color online) Driving point impedance at the base of an attached rod. Normalized mode shapes of Eq. (1) of the displacement for a unit force are shown by the colored long rectangles located at the frequencies corresponding to the mode. The color bar for these displays is shown on the right. As can be seen, the first, third, and fifth modes have no displacement at the attachment point.

The physical parameters of the aluminium beam and rods are, for the beam, $\rho = 2700$, thickness $h = 0.006$, width $b = 0.02$, area $A = hb$, Young's modulus $E = 69 \times 10^9$, moment of area $I = h^3 b/12$; and for the circular rod also made of aluminium, length $L_b = 0.61$, diameter $d = 0.006\,35$. The distance (L) between adjacent rods was $L = 0.02$.

A. The resonant element: A longitudinally vibrating rod

We define the unit cell for our problem as a beam segment of length L with a single homogeneous rod (shown in Fig. 3 as the vertical segment along the y axis) attached to the middle of the segment. We restrict the vibration of the rod to extensional, in-plane motion and ignore the out-of-plane flexural motion of the rod. Given the thickness of the beam this has proven to be a good assumption. The boundary conditions for the rod are free at one end ($y = L_b$) and at the other end ($y = 0$) driven by a longitudinal force F in the positive y direction, the force exerted due to the attachment to the beam. The solution for the longitudinal displacement $u_b(y)$ along a rod of length L_b and area A_b is, with time convention $e^{-i\omega t}$ and wave number $k_b \equiv \omega/c_b$,

$$u_b(y) = \frac{-F}{\omega \rho_b A_b c_b} \left[\sin(k_b y) + \frac{\cos(k_b L_b)}{\sin(k_b L_b)} \cos(k_b y) \right]. \quad (1)$$

The nondispersive wave velocity in the rod with Young's modulus E_b and density ρ_b is given by $c_b = \sqrt{E_b/\rho_b}$ (5055 m/s). The driving force obeys $F = -E_b A_b \frac{\partial u_b}{\partial y}$ where A_b is the cross-sectional area and $-\frac{du_b}{dy}$ is the compression. The driving point impedance $Z_b \equiv F/[-i\omega u_b(0)]$ is

$$Z_b = -i\rho_b A_b c_b \tan(k_b L_b), \quad (2)$$

which is plotted versus frequency in Fig. 4. We also show in this figure a group of vertical slices corresponding to the

displacement along the rod color coded as shown by the color bar on the right.

We define a resonance to correspond to the case where the admittance $1/Z_b = v/F \to \infty$ (v is velocity), that is, the *velocity at either end of the rod is a maximum per unit applied force*. Reference to the figure shows that this occurs for the second and fourth displacement shapes. We define an antiresonance as $Z_b \to \infty$ corresponding to the case when *the drive point becomes motionless*, corresponding to the first, third, and fifth displacement shapes. We expect the motionless case to be important as our goal is the cancellation of the motion at the base of the rod forest. It is the antiresonance of the rods in the forest that tends to clamp the motion of the plate beneath, with the multitude of rods amplifying this effect. We find in the analysis below that indeed the antiresonance frequency forms the beginning of the stop bands that arise. The first antiresonance frequency of the rod ($Z_b \to \infty$ and $u_b(0) \to 0$) is $\omega L_b/c_b = \pi/2$, that is, $\omega_0 = \pi c_b/(2L_b)$. The first three antiresonances occur at 2.063, 6.190, and 10.320 kHz (see Fig. 4).

Finally, the impedance of the rod indicates, given the time dependence, that it is masslike in the regions where $\Im(Z_b) < 0$ and springlike when $\Im(Z_b) > 0$ ($\Im$ is the imaginary part), which we will find correspond to the passbands and stop bands, respectively.

B. Scattering matrix derivation: Transversally vibrating beam with resonant rods

We now consider the plate substrate modeled as a transversally vibrating beam. The classic equation of motion for the out-of-plane displacement $u(x)$ of a beam with an external force f_b (positive upwards) and a moment m_b applied at $x = x_0$ at the point of attachment of the rod is

$$EI\frac{\partial^4 u(x)}{\partial x^4} - \rho A\omega^2 u(x) = f_b\delta(x - x_0) - m_b\delta'(x - x_0). \tag{3}$$

The out-of-plane *velocity* is given by $v(x) = -i\omega u(x)$. The experimental results have shown that we can assume that rotational coupling via m_b is small in comparison to f_b and we can set $m_b = 0$.

The bending moment and shear force internal to the beam satisfy $M(x) = -EI\frac{\partial^2 u}{\partial x^2}$ and $F(x) = -\frac{\partial M(x)}{\partial x}$. The dispersive wave number that results from the homogeneous solution of Eq. (3) is given by

$$k = \left(\frac{\rho A\omega^2}{EI}\right)^{1/4}. \tag{4}$$

If we write $k = \omega/c_p$ then flexural waves travel at a speed given by

$$c_p = \sqrt{\omega}\left(\frac{EI}{\rho A}\right)^{1/4}. \tag{5}$$

At the attachment point x_0 of the rod the force balance is $f_b = -F = -Z_b v(x_0)$ where $v(x_0)$ is the out-of-plane velocity of the beam at the drive point and Z_b is given in Eq. (2).

As shown in Fig. 3 we approach the solution by studying the transmission properties of a single cell using a wave approach that models the physics. According to thin plate-beam theory the beam supports two wave types, flexural and evanescent. These are solutions of the homogeneous form of Eq. (3), the right- and left-going plane (flexural) waves $e^{\pm ikx}$ and the right- and left-going evanescent (decaying) waves $e^{\mp kx}$. The wave decomposition for the nth segment is shown in the figure. This wave approach allows the consideration of just a single beam or rod segment, which we call a unit cell, leading to the generation of a matrix expression that can be used to fully describe the physics at play in the segment. The incident and reflected waves inside this unit cell embody the multiple reflection or transmission events of the rod forest. This approach leads to the scattering matrix (or T matrix) for the cell and is completely analogous to those found in the literature (Lagarrigue [21], Wu [9], Liu) [8], etc.).

In the analysis to follow we will assume that kL is of the order unity or less, so that many rods are contained within a flexural wavelength, $\lambda_f = 2\pi/k$, a critical condition for the creation of a metamaterial.

Considering one segment, let $u(x)$ represent the displacement of the beam on the left side of the rod ($-L/2 \leqslant z < 0$), and $w(x)$ the displacement of the right side ($0 < z \leqslant L/2$) of the rod (which is assumed to have no width). We decompose these displacement functions into the waves that form the homogeneous solution of Eq. (3):

$$u(x) = u^{(n)}(x) = u_r^{(n)}e^{ikx} + u_\ell^{(n)}e^{-ikx} + u_{re}^{(n)}e^{-kx} + u_{\ell e}^{(n)}e^{kx}, \tag{6}$$

$$w(x) = w^{(n)}(x) = w_r^{(n)}e^{ikx} + w_\ell^{(n)}e^{-ikx} + w_{re}^{(n)}e^{-kx} + w_{\ell e}^{(n)}e^{kx}, \tag{7}$$

indicated in Fig. 3. We treat the amplitudes of the waves incident towards the rod as independent variables, that is, $w_\ell^{(n)}, w_{\ell e}^{(n)}, u_r^{(n)}, u_{re}^{(n)}$, the reflected waves as dependent variables, *viz.*, $w_r^{(n)}, w_{re}^{(n)}, u_\ell^{(n)}, u_{\ell e}^{(n)}$. The subscript r refers to right-going and ℓ to left-going, as the arrows indicate in the figure. The extra subscript e refers to an evanescent wave type, and the superscript refers to the segment number.

Solution of the problem of the wave transmission through the forest of rods requires setting up two conditions. The first is the local boundary condition at the rod, which embodies the interaction physics of the rod to beam attachment. For this we derive the scattering matrix S relating outgoing to incoming waves, and reorder it to form a wave coupling matrix C that we describe later. The second is the requirement that the wave propagation must be continuous at the boundary between any two adjacent cells. That is, for example, on the left end of the nth segment $u^{(n)}(-L/2)$ is equal to $w^{(n-1)}(L/2)$ the displacement at the right end of the abutting segment [see Eqs. (6) and (7)]. The waves coming from, or reflected to, the $n-1$th segment are continuous with those of the adjacent nth segment.

We first consider the derivation of the scattering matrix S of Eq. (8) below. The physics dictates that when the incident field of amplitude u_r encounters the left end of the rod it produces four events: a transmitted flexural wave of amplitude $w_r = tu_r$ (where t is the transmission coefficient), a transmitted evanescent wave $w_{re} = t_{fe}u_r$ (flexural to evanescent transmission coefficient t_{fe}), a reflected flexural wave $u_\ell = ru_r$, and a reflected evanescent wave $u_{\ell e} = r_{fe}u_r$. Furthermore, the incident evanescent field u_{re} also produces the same four junction events, but possibly with different reflection and

transmission coefficients. We impose a symmetric system: the wave entering from the right encounters the same reflection and transmission coefficients as the wave entering from the left. Thus we write the matrix system relating outgoing (scattered) to incoming waves at the rod (the scattering matrix S):

$$\begin{pmatrix} u_\ell^{(n)} \\ u_{\ell e}^{(n)} \\ w_r^{(n)} \\ w_{re}^{(n)} \end{pmatrix} = \begin{pmatrix} r & r_{ef} & t & t_{ef} \\ r_{fe} & r_e & t_{fe} & t_e \\ t & t_{ef} & r & r_{ef} \\ t_{fe} & t_e & r_{fe} & r_e \end{pmatrix} \begin{pmatrix} u_r^{(n)} \\ u_{re}^{(n)} \\ w_\ell^{(n)} \\ w_{\ell e}^{(n)} \end{pmatrix}$$

$$\equiv (S) \begin{pmatrix} u_r^{(n)} \\ u_{re}^{(n)} \\ w_\ell^{(n)} \\ w_{\ell e}^{(n)} \end{pmatrix}. \tag{8}$$

We determine the matrix S in Eq. (8) by setting up the boundary conditions on either side of the rod. For coupling of the rod to the beam, ignoring transverse motion of the rod as discussed above, the boundary conditions on either side of the rod are equality of displacement, slope, and curvature, and a jump condition in the third derivative given by the shear force reaction of the rod:

$$\begin{aligned} u(0^-) &= w(0^+), \\ u'(0^-) &= w'(0^+), \\ u''(0^-) &= w''(0^+), \\ w'''(0^+) - u'''(0^-) &= \frac{i\omega Z_b}{EI} u(0^-). \end{aligned} \tag{9}$$

Applying these boundary conditions to Eqs. (6) and (7) and solving for the left-hand side of Eq. (8) using MATHEMATICA, we obtain

$$r = \frac{i\Theta}{1+(1-i)\Theta}, \quad t = \frac{1+\Theta}{1+(1-i)\Theta}, \tag{10}$$

$$r_e = \frac{-\Theta}{1+(1-i)\Theta}, \quad t_e = \frac{1-i\Theta}{1+(1-i)\Theta}, \tag{11}$$

$$r_{fe} = \frac{-\Theta}{1+(1-i)\Theta}, \quad r_{ef} = \frac{i\Theta}{1+(1-i)\Theta}, \tag{12}$$

$$t_{ef} = \frac{i\Theta}{1+(1-i)\Theta}, \quad t_{fe} = \frac{-\Theta}{1+(1-i)\Theta}, \tag{13}$$

where Θ is unitless and purely real defined by $\Theta \equiv i\omega Z_b/(4EIk^3)$. Another useful definition that eliminates EI, using Eqs. (4) and (2), is

$$\Theta = \frac{1}{4} \frac{\rho_b A_b c_b}{\rho A c_p} \tan(k_b L_b). \tag{14}$$

From Eq. (10) we see that $t = 1 + r$ and $t_e = 1 + r_e$.

At resonance $\Theta \to 0$, where the condition is equivalent to no rod attached, the above expressions show that $r = r_e = r_{fe} = r_{ef} = 0$ and $t = t_e = 1$ and $t_{ef} = t_{fe} = 0$ as we expect. There are no reflections, no coupling between evanescent and plane (flexural), and unit transmissions.

Although the scattering matrix S is fundamental to 2D mathematical approaches discussed above, our 1D approach is better served by defining a new matrix C that we call the coupling matrix that treats the left-side wave amplitudes as the independent variables instead of the incoming wave amplitudes, *viz.,*

$$W^{(n)} = CU^{(n)}, \tag{15}$$

with the right-side vector of amplitudes $W^{(n)} \equiv (w_\ell^{(n)}, w_{\ell e}^{(n)}, w_r^{(n)}, w_{re}^{(n)})^t$ and left-side vector $U^{(n)} \equiv (u_\ell^{(n)}, u_{\ell e}^{(n)}, u_r^{(n)}, u_{re}^{(n)})^t$ (t is transpose). Note that these vectors just correspond to a reordering of the column vectors of Eq. (8). The resulting remarkably simple coupling matrix C is

$$C = \begin{bmatrix} 1-i\Theta & -i\Theta & -i\Theta & -i\Theta \\ \Theta & \Theta+1 & \Theta & \Theta \\ i\Theta & i\Theta & i\Theta+1 & i\Theta \\ -\Theta & -\Theta & -\Theta & 1-\Theta \end{bmatrix}. \tag{16}$$

C. Formulation for the transmission matrix

Having satisfied the boundary conditions at the rod, we now consider the requirement of continuity of displacement between two adjacent cells. Using Eqs. (6) and (7) we can define a displacement vector at the right end of the nth beam segment $W_+^{(n)}$ and $U_-^{(n)}$ at the left end, at distance $L/2$ from the rod:

$$W_+^{(n)} = DW^{(n)}, \tag{17}$$

$$U_-^{(n)} = D^{-1}U^{(n)}, \tag{18}$$

with

$$D \equiv \begin{bmatrix} e^{-ikL/2} & 0 & 0 & 0 \\ 0 & e^{kL/2} & 0 & 0 \\ 0 & 0 & e^{ikL/2} & 0 \\ 0 & 0 & 0 & e^{-kL/2} \end{bmatrix}. \tag{19}$$

The continuity condition between the two adjacent segments is then given by $U_-^{(n)} = W_+^{(n-1)}$, the wave amplitudes being equal at the junction. Using this condition in Eqs. (17) and (18) along with Eq. (15) yields the final coupling relationship:

$$W_+^{(n)} = DCDW_+^{(n-1)}. \tag{20}$$

We define DCD in this equation as a transfer matrix T, $T \equiv DCD$, and find that

$$T = \begin{pmatrix} e^{-ikL}(1-i\Theta) & -ie^{(\frac{1}{2}-\frac{i}{2})kL}\Theta & -i\Theta & -ie^{(-\frac{1}{2}-\frac{i}{2})kL}\Theta \\ e^{(\frac{1}{2}-\frac{i}{2})kL}\Theta & e^{kL}(1+\Theta) & e^{(\frac{1}{2}+\frac{i}{2})kL}\Theta & \Theta \\ i\Theta & ie^{(\frac{1}{2}+\frac{i}{2})kL}\Theta & e^{ikL}(1+i\Theta) & ie^{(-\frac{1}{2}+\frac{i}{2})kL}\Theta \\ -e^{(-\frac{1}{2}-\frac{i}{2})kL}\Theta & -\Theta & -e^{(-\frac{1}{2}+\frac{i}{2})kL}\Theta & e^{-kL}(1-\Theta) \end{pmatrix}. \tag{21}$$

We proceed by carrying out an eigensystem analysis of T.

D. Eigenanalysis

The eigendecomposition of T is $T = V\Lambda V^{-1}$ where Λ is the diagonal matrix of eigenvalues, λ_i. Consider the total wave propagation through a rod forest of N segments. Although it is not necessary for our analysis we can insert the driving condition of the system in the left end, an incident nonevanescent wave of unity amplitude, by letting the input vector be $W_+^{(0)} = (w_\ell^{+(0)}, w_{\ell e}^{+(0)}, 1, 0)^t$. At the right end the output vector is $W_+^{(N)} = (0, 0, w_r^{+(N)}, w_{re}^{+(N)})^t$ assuming no incident waves from the right. We will not need these conditions, however, in what follows.

The general relationship between the input and output vectors is

$$W_+^{(N)} = T^N W_+^{(0)} = V\Lambda^N V^{-1} W_+^{(0)} = B W_+^{(0)}, \tag{22}$$

where N is the number of sections and $B \equiv T^N = V\Lambda^N V^{-1}$.

An eigenanalysis of Eq. (21) can yield the eigenvalues Λ directly. We obtain from a MATHEMATICA evaluation that the eigenvalues λ_i are solutions of the following equation:

$$\lambda^4 - 2c_1\lambda^3 + d_1\lambda^2 - 2c_1\lambda + 1 = 0, \tag{23}$$

with

$$c_1 \equiv \Theta[\sinh(kL) - \sin(kL)] + \cos(kL) + \cosh(kL), \tag{24}$$

$$d_1 \equiv 4\Theta[\cos(kL)\sinh(kL) - \sin(kL)\cosh(kL)] + 4\cosh(kL)\cos(kL) + 2. \tag{25}$$

As a sanity check, when $\Theta = 0$, $c_1 = d_1 = 0$, and we obtain $\lambda_i = \{e^{kL}, e^{ikL}, e^{-ikL}, e^{-kL}\}$, as expected.

In general we express the eigenvalues through their exponential representations,

$$\lambda_p = e^{\pm ib}, \tag{26}$$

for the passband, which exhibits $|\lambda_p| = 1$, and in the stop band,

$$\lambda_s = e^{\pm(a \pm ib)}, \tag{27}$$

which exhibits an attenuation given by $|\lambda_s| = e^{-|a|}$. We can also write the latter in terms of an attenuation coefficient per unit length $\alpha(\omega)$, $e^{-|a|} = e^{-\alpha(\omega)L}$ where $\alpha \equiv |a|/L$. The four roots determined from the solution of Eq. (23) are plotted and discussed at the beginning of the Appendix.

Critical to our analysis and the metamaterial characterization is the assumption that there are many beam segments within the A_0 mode flexural wavelength, corresponding mathematically to the condition that kL is of order unity or smaller. Thus we develop an expansion of Eqs. (24) and (25) in kL retaining the dominant terms (see Appendix). We find that, from Eq. (A15) of the Appendix and keeping only the first term, for the passband given by $\tilde{\Xi} > 0$,

$$\lambda_p \approx e^{\pm i\sqrt{2}(3\tilde{\Xi})^{1/4}}, \tag{28}$$

and for the stop band ($\tilde{\Xi} < 0$) we obtain from Eqs. (A16) and (A17)

$$\lambda_s \approx e^{-(3|\tilde{\Xi}|)^{1/4}} e^{\pm i(3|\tilde{\Xi}|)^{1/4}}, \tag{29}$$

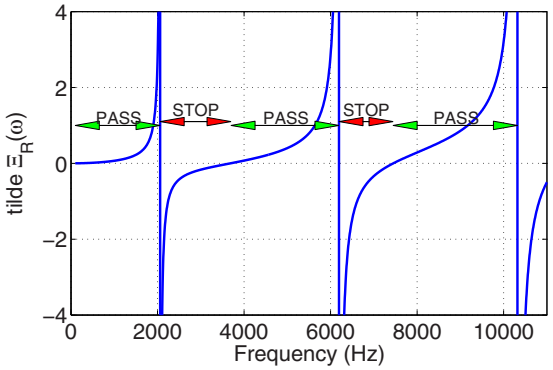

FIG. 5. (Color online) Plot of $\tilde{\Xi}$ versus frequency for the parameters of the experiment. Compare with Fig. 8. It is infinite at the antiresonances 2063 and 6190 Hz. The junctions between the stop and passband are at 3700 and 7450 Hz, at the point where $\tilde{\Xi} = 0$. The arrows indicate where the passbands and stop bands are located in the frequency spectrum.

where

$$\tilde{\Xi} = \frac{(kL)^4}{12}\left[\frac{M_b}{M}\frac{\tan(k_bL_b)}{k_bL_b} + 1\right], \tag{30}$$

in which M_b is the total mass of a rod and M the mass of the beam segment of length L. Figure 5 is a representative plot of $\tilde{\Xi}$ for the physical parameters of the experiment, with $M_b/M = 8.02$. The passbands and stop bands defined by Eqs. (28) and (29) are indicated in this figure.

From Eqs. (30) and (29) we see that the stop band attenuation coefficient is given by

$$\alpha(\omega) = \frac{(3|\tilde{\Xi}|)^{1/4}}{L} = \frac{k}{\sqrt{2}}\left|\frac{M_b}{M}\frac{\tan(k_bL_b)}{k_bL_b} + 1\right|^{1/4}. \tag{31}$$

Analysis of the attenuation indicates that the attenuation is infinite at the antiresonances of the rod (given by $\tan \to \pm\infty$ or $k_bL_b = \pi/2, 3\pi/2$) and that these frequencies mark the onset of the stop bands, shown in Fig. 5. Thus at the onset of the stop bands the Lamb wave attempting to pass through a segment experiences an extremely high attenuation due to the longitudinal antiresonances of the attached rod. These antiresonances clamp the motion of the beam. As the frequency increases, Eq. (31) indicates that the attenuation coefficient decreases to zero at the end of the stop band since $\tilde{\Xi} \to 0$. Of course, the decay through a forest of N rods is given by λ^N resulting from the eigenanalysis, with an attenuation of $e^{Na} = e^{-N\alpha L}$ in the distance NL. We will show the comparison to the experimental results later in this paper.

Consider the propagation in the passband defined by $\tilde{\Xi}(\omega) > 0$ and given by Eqs. (28) and (26) with the phase factor $b = \sqrt{2}(3\tilde{\Xi})^{1/4}$. It is straightforward to homogenize the rod forest and seek the solution for a right-going A_0 Lamb wave of unity amplitude passing through it with an effective (modified) wave number modeled after the plane wave solution for an infinite beam made out of the homogenized effective medium [*viz.,* given by Eq. (3) in homogeneous form and Eq. (4) with $k \to k_{\text{eff}}$]:

$$u_{\text{eff}}(x) = e^{ik_{\text{eff}}x}.$$

The evanescent wave solution of Eq. (3) is irrelevant for this characterization due to its decay. We can model the traveling wave propagation through a segment of the beam using the effective wave number $k_{\text{eff}}(\omega)$ as $e^{ik_{\text{eff}}x} = e^{ib(\omega)x/L}$ yielding $k_{\text{eff}} = b(\omega)/L$. Using Eqs. (28) and (30) we find that

$$k_{\text{eff}}(\omega) \approx k\left[\frac{M_b}{M}\frac{\tan(k_bL_b)}{k_bL_b}+1\right]^{1/4}, \tag{32}$$

where $k(\omega)$ is from Eq. (4) as before. Thus the term in Eq. (32) with the $1/4$ power displays the change in wave number due to the metamaterial. $k_{\text{eff}}(\omega)$ yields a new dispersion relation that fully characterizes the metamaterial. We will compare this with that determined from the experiment in the next section, the major objective of this paper.

We can also define an effective wave speed c_{eff} from Eq. (32) given by

$$c_{\text{eff}}/c_p = \left[\frac{M_b}{M}\frac{\tan(k_bL_b)}{k_bL_b}+1\right]^{-1/4}. \tag{33}$$

Figure 5 shows that at the beginning of the passband $\Xi = 0$ so that $c_{\text{eff}} \to \infty$, whereas at the end of the passband $c_{\text{eff}} \to 0$.

In the characterization of metamaterials there is a large volume of literature describing them as having negative mass density and/or negative compressibility in the stop bands. Generally this relationship is made using monopole and dipole expansions of the metamaterial element (our rod), which is assumed elastic through its cross section. The monopole (breathing mode of the cross section) relates to negative compressibility and the dipole (lateral displacement of the cross section) to negative density. See, for example, Wu [9]. In our case, however, the rod is modeled as a *point* attachment, and the force it applies to the plate is omnidirectional and thus monopole-like in its excitation of A_0 waves. Since in-plane, longitudinal S_0 waves in the plate are not excited, there is no dipole-like excitation, and the result is a monomodal system, unlike Wu's case. Because of this we can characterize the metamaterial as having negative density or compressibility, but not both in the stop band. The effective density ρ_{eff} can can be formulated from the effective wave number, derived from Eq. (29) for the stop band,

$$k_{\text{eff}}=(\pm 1+i)\frac{k}{\sqrt{2}}\left|\frac{M_b}{M}\frac{\tan(k_bL_b)}{k_bL_b}+1\right|^{1/4}=\left(\frac{\rho_{\text{eff}}A\omega^2}{EI}\right)^{1/4}. \tag{34}$$

Using Eq. (4) for k we then obtain the negative effective density

$$\rho_{\text{eff}} = -\rho\left|\frac{M_b}{M}\frac{\tan(k_bL_b)}{k_bL_b}+1\right|.$$

However, we could have derived an effective Young's modulus E_{eff} instead, keeping the density unchanged, which would similarly result in a negative effective modulus: a negative compressibility. There does not appear to be a unique characterization in our case.

III. EXPERIMENTAL RESULTS

The experimental setup was shown in Fig. 1. A recent publication (Rupin) [19] described the setup and measurement which we summarize here. The aluminum plate with a chaotic shape (1.5 m × 2.0 m) was excited by a pulsed shaker mounted perpendicular to the plate surface, exciting the antisymmetric A_0 flexural wave mode of the plate. The vibration of the plate along a strip [labeled (5) in the figure] is measured with a Doppler velocimeter using a PC-controlled motorized mirror with output correlated to the driving pulse on the shaker. At the right of the scanned rectangle is a metamaterial fashioned with a set of 100 cylindrical rods glued on a 0.2 m by 0.2 m area and located underneath the plate.

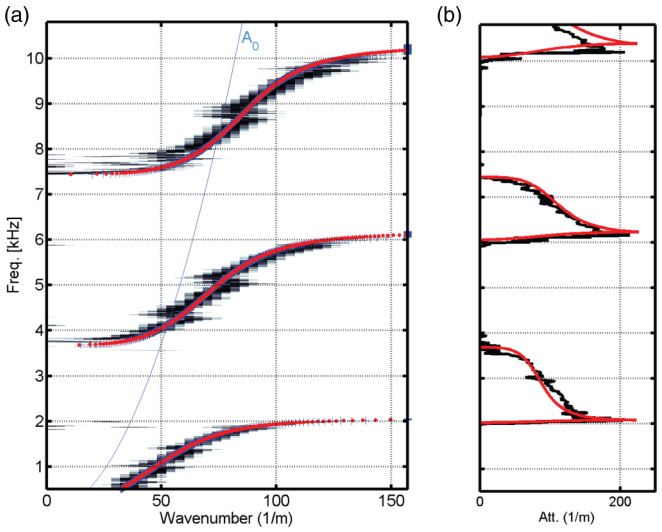

FIG. 6. (Color online) Experimental versus theoretical dispersion curve for the multiresonant metamaterial. On the left (a) is shown the experimental wave number (black) superimposed with the effective wave number (blue plus) from the solution of Eq. (23) and approximate (red dot) formula from Eq. (32). On the right (b) is the attenuation through 10 rods measured (black) and calculated from Eq. (23) (red) in the stop bands. The agreement is excellent between the theory and the experiment.

The experimentally measured dispersion curve inside the metamaterial was computed from the velocimeter scan and a 2D spatial Fourier transform calculated as a function of frequency yielding a frequency-wave number dispersion curve using a radial averaging process.

The dispersion relation is shown by the black curves in Fig. 6 with effective wave number on the left and attenuation (β) on the right. The attenuation is measured by matching the decay of the spatial intensity of the data to $e^{-\beta x}$ at each stop band frequency in the metamaterial. The solid blue line labeled A_0 is k from Eq. (4) for the plate without rods.

The results of the 1D theory developed in this paper are plotted in Fig. 6(a) with the result of Eq. (32), the effective wave number keff in the passband, plotted with the dotted red curve on the left and the attenuation in the stop band $\beta = -2\log|\lambda|/L$ from Eq. (27) using a solid red curve on the right [Fig. 6(b)]. The agreement between experiment and theory is excellent.

Also plotted with a blue + curve on the left of Fig. 6 is the exact solution for k_{eff} generated by finding the exact roots of Eq. (23). This curve falls on top of the approximation (red dots). Indeed, it shows that the simple approximation for the roots given in the Appendix is very accurate for this case. In

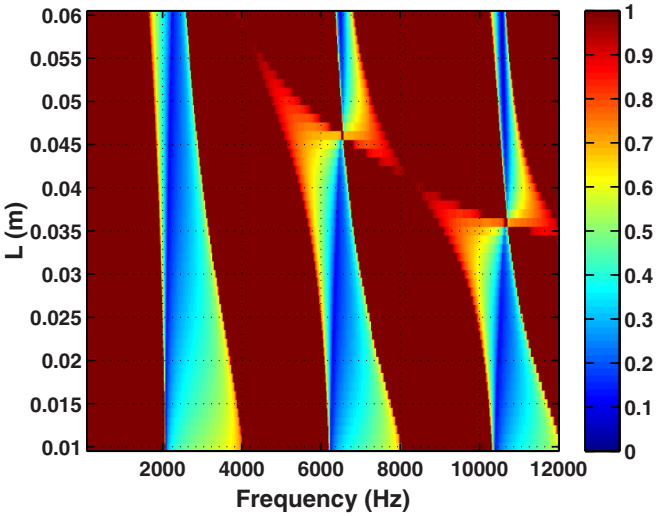

FIG. 7. (Color online) Passband and stop band structure versus kL. Dark red represents the passband $|\lambda_p| = 1$, and the stop band attenuation is shown in the color bar $|\lambda_s|$ computed from the exact solution of Eq. (23).

terms of the kL expansions, we note that at 10 kHz we have $kL = 1.69$, with one term in the expansion still sufficient.

The dispersion result in Fig. 6 explains the effective wavelengths observed in the wave field maps at the various frequencies in Fig. 2. The phase velocity ($c_p = \omega/k$) of the waves outside the metamaterial (abscissa 0.2 to 1.2 in the plots) is dictated by the A_0 curve in Fig. 6. The effective phase velocity within the metamaterial is governed by $c_{\text{eff}} = \omega/k_{\text{eff}}$, so that when $k_{\text{eff}} < k$ the phase velocity is faster and the resulting wavelength in the metamaterial larger than outside. Conversely, when $k_{\text{eff}} > k$ the phase velocity is less and the wavelength is smaller in the metamaterial. These two cases are shown in the bottom plot (7512 Hz, larger wavelength in the metamaterial) and in the top plot (5808 Hz, smaller wavelength in the metamaterial), respectively. Finally the middle plot (6567 Hz) shows the result in the stop band; there is no penetration of waves into this region.

An interesting question arises: as the spacing between the rods increases, at what point does the medium fail to be a metamaterial, failing to generate stop bands? To illuminate the answer we ran a simulation, changing the spacing between the rods and using the exact solution from Eq. (23) to predict the passband and stop band generation. Figure 7 is a plot of $|\lambda|$ from the exact solution over values of $.01 \leqslant L \leqslant .06$ to indicate the change of the band structure. The passband is the red regions $|\lambda| = 1$, according to the color map. We can see that the stop bands narrow as L increases, and stop bands begin to disappear as there are fewer and fewer rods contained within a flexural wavelength. The bifurcation seen in the upper right of the plot occurs at $kL = \pi$ corresponding a half flexural wavelength between the rods.

IV. IRREGULAR SPACING OF THE ATTACHED RODS

Finally we turn to the observation given in Rupin *et al.* (2014) that the passbands and stop bands develope independent of the arrangement of the rod forest, that is, regular grid versus random spacing. Consider the question "does irregular spacing of the distances between the rods change the stop or passband frequencies of the system?" If we assume that the irregular spacing is random, small compared to L with zero mean, then the answer appears to be no, as we now show.

Assume that the length of a the ith beam segment $\tilde{L}_i$ is perturbed by a small amount δx_i such that $k\tilde{L}_i = kL + k\delta x_i$ and define $\epsilon_i = k\delta x_i$ where we assume that the Gaussian random number $\epsilon_i \ll 1$ with zero mean and standard deviation $\sigma \ll 1$. The diagonal matrix D of Eq. (17) is defined for the ith segment using $\tilde{L}_i$ instead of L as $\tilde{D}_i$:

$$\tilde{D}_i = \begin{pmatrix} e^{-ik\tilde{L}_i/2} & 0 & 0 & 0 \\ 0 & e^{k\tilde{L}_i/2} & 0 & 0 \\ 0 & 0 & e^{ik\tilde{L}_i/2} & 0 \\ 0 & 0 & 0 & e^{-k\tilde{L}_i/2} \end{pmatrix}.$$

Since $k\tilde{L}_i = kL + \epsilon_i$, and keeping terms to second order, $e^{\epsilon} \approx 1 + \epsilon + \epsilon^2/2$ we can approximate the last equation as

$$\tilde{D}_i \approx D\left(I + \epsilon_i \underbrace{\begin{pmatrix} -i/2 & 0 & 0 & 0 \\ 0 & 1/2 & 0 & 0 \\ 0 & 0 & i/2 & 0 \\ 0 & 0 & 0 & -1/2 \end{pmatrix}}_{I'} + \epsilon_i^2 \underbrace{\begin{pmatrix} -1/8 & 0 & 0 & 0 \\ 0 & 1/8 & 0 & 0 \\ 0 & 0 & -1/8 & 0 \\ 0 & 0 & 0 & 1/8 \end{pmatrix}}_{I''} \right)$$
$$= D\left(I + \epsilon_i I' + \epsilon_i^2 I''\right),$$

where I is the unit diagonal, $I' = 1/2\ \text{diag}[\{-i,1,i,-1\}]$ and $I'' = 1/8\ \text{diag}[\{-1,1,-1,1\}]$. If we consider N segments then in Eq. (22), B is replaced by

$$\tilde{B} = \prod_{i=1}^{N} (\tilde{D}_i C \tilde{D}_i) \approx \prod_{i=1}^{N} \left(I + \epsilon_i I' + \epsilon_i^2 I''\right) T \left(I + \epsilon_i I' + \epsilon_i^2 I''\right)$$
$$\approx \prod_{i=1}^{N} \left(T + \epsilon_i I' T + \epsilon_i T I' + \epsilon_i^2 I' T I' + \epsilon_i^2 I'' T + \epsilon_i^2 T I''\right) = \prod_{i=1}^{N} \left(T + \epsilon_i F + \epsilon_i^2 G\right),$$

where $T = DCD$ [see Eq. (21)], $F = I'T + TI'$, $G = I'TI' + I''T + TI''$, dropping terms of third and fourth order. Consider the first two terms in the product, again keeping terms only in ϵ^2:

$$T^2 + \epsilon_1 FT + \epsilon_1^2 GT + \epsilon_2 TF + \epsilon_1\epsilon_2 F^2 + \epsilon_2^2 TG.$$

The ensemble average of terms with ϵ_i alone will be zero, and terms with the cross products $\epsilon_i\epsilon_j$ $(i \neq j)$ zero also, with the ϵ_i^2 terms averaging to σ^2. To build a general rule, consider the ensemble average of the product of four terms ($N = 4$):

$$\left\langle \prod_{i=1}^{4} \left(T + \epsilon_i F + \epsilon_i^2 G\right) \right\rangle = T^4 + GT^3\sigma^2 + TGT^2\sigma^2 + T^2GT\sigma^2 + T^3G\sigma^2.$$

For N terms by induction we obtain

$$\langle \tilde{B} \rangle = \left\langle \prod_{i=1}^{N} \tilde{D}_i C \tilde{D}_i \right\rangle \approx T^N + \sigma^2 \sum_{k=1}^{N} T^{k-1} G T^{N-k}. \quad (35)$$

To determine that the summation term in Eq. (35) is not significant consider the L2 norm ($\|\cdot\|$) and use the matrix norm rules $\|AB\| \leqslant \|A\|\|B\|$ and $\|A + B\| \leqslant \|A\| + \|B\|$,

$$\left\| \sum_{k=1}^{N} T^{k-1} G T^{N-k} \right\| \leqslant \sum_{k=1}^{N} \|T^{k-1}\|\|G\|\|T^{N-k}\| \leqslant \frac{N}{2}|\lambda|^N,$$

since $\|G\| \leqslant \frac{1}{2}\|T\|$ and $\|T\| = |\lambda|$ where $|\lambda|^2$ is the maximum singular value of $T^H T$. Finally the size of $\langle \tilde{B} \rangle$ is

$$\|\langle \tilde{B} \rangle\| \leqslant |\lambda|^N + \sigma^2 \frac{N}{2}|\lambda|^N \approx \left[|\lambda|\left(1 + \frac{\sigma^2}{2}\right)\right]^N,$$

from which we conclude that the largest eigenvalue is increased by a negligible amount when $\sigma \ll 1$. Furthermore we conclude from Eq. (35), having considered terms up to second order in ϵ_i, that $\langle \tilde{B} \rangle \approx T^N = B$; the randomly disordered lattice yields the same transfer matrix (in Eq. (22)) as the original regular lattice, and the eigenvalues, passbands, and stop bands remain essentially unchanged.

V. CONCLUSIONS

Plates support two types of waves at low frequencies: the symmetric and antisymmetric modes, S_0 and A_0. In practice, A_0 waves are mostly vertically polarized and can be characterized by out-of-plane (vertical) displacement when in-plane (horizontal) displacements in the plate are described by S_0 waves. Numerical simulations performed with 3D elastic finite-element code in the plate + metamaterial confirm that nearly no energy is present in the S_0 mode (Colombi) [22]. This means that the potential conversion of the excited A_0 waves to S_0 modes upon scattering of the resonating beams can be neglected in the present configuration. Indeed, given the plate thickness (6 mm), the flexural resonances of the beams are weakly excited by the A_0 incident wave, and we can limit the analysis to the interaction between the A_0 mode and the longitudinal resonances inside the beams. We expect things to be very different with a thinner plate (i.e., more flexible), where both A_0 and S_0 modes may be excited at the interface between plate and beams. In such a case, both flexural and compressional resonances may modify the band gap structure, which would require to add the in-plane component to the theoretical approach. This case is the object of current research.

The results in Fig. 6 show that a 1D theory has been extremely successful at predicting the 2D scattering from a rectangular patch of 10×10 rods attached to the surface of a plate with a dispersive boundary shape. The experimental dispersion curve is computed during the reverberant coda of the time series, eliminating the direct contribution. However, we must conclude from the agreement between the 1D theory and the 2D experiment that the metamaterial properties create a scattering event that is not incident angle dependent in both the passbands and the stop bands.

Significant is the high level of attenuation obtained by a relatively small number of rods with each rod providing 20 dB of attenuation at the beginning of the stop band. Thus one could consider a distribution of smaller patches of rods, tuned differently in each patch to extend the stop band over a broader frequency range.

With the extremely simple yet highly accurate relations given by Eqs. (28) and (29) to predict the passband and stop band characteristics of the metamaterial, we have a tool to develop more complex metamaterials with rods of different properties to provide more precise control of the Lamb wave propagation. That is, the transfer matrix approach described here [Eq. (21)] can be generalized to unit cells with different size and properties (longer or smaller rods of different materials, for example). Each unit cell k corresponds to a transfer matrix A_k and the full transfer matrix for a metamaterial made of N cells is the product $A_{\text{tot}} = A_1 \times \cdots \times A_N$ (see for example Gilbert [23], Schoenberg and Sen) [24] as already shown for irregular spacing between bars in this paper (Sec. IV). For example, this propagation matrix method has already been applied to a variable layered media to construct a metamaterial with an effective density tensor (see, for example, Cheng) [25] to realize the cloaking parameters specified by Pendry [26] and Leonhardt [27]. We therefore expect the rod-plate system to be amenable to analogous applications.

ACKNOWLEDGMENTS

E.G.W. acknowledges support from the Office of Naval Research.

APPENDIX

The four roots determined from the solution of Eq. (23) for the parameters of the plate experiment, using the MATLAB roots function are plotted versus frequency in Fig. 8. The magnitude of the third root $|\lambda_3|$ shown in red, exhibits the passband and stop band character that we seek. It is important to note that the eigenvalues must represent the symmetry of the wave propagation; that is, we have not specified from which direction the initial excitation comes. Thus in the stop band the inverse of the third eigenvalue $|1/\lambda_3|$ is exactly equal to $|\lambda_1|$.

For the derivation of Eqs. (28) and (29) we define

$$\beta_{\pm} = \tfrac{1}{2}\left[c_1 \pm \left(2 + c_1^2 - d_1\right)^{1/2}\right], \quad (A1)$$

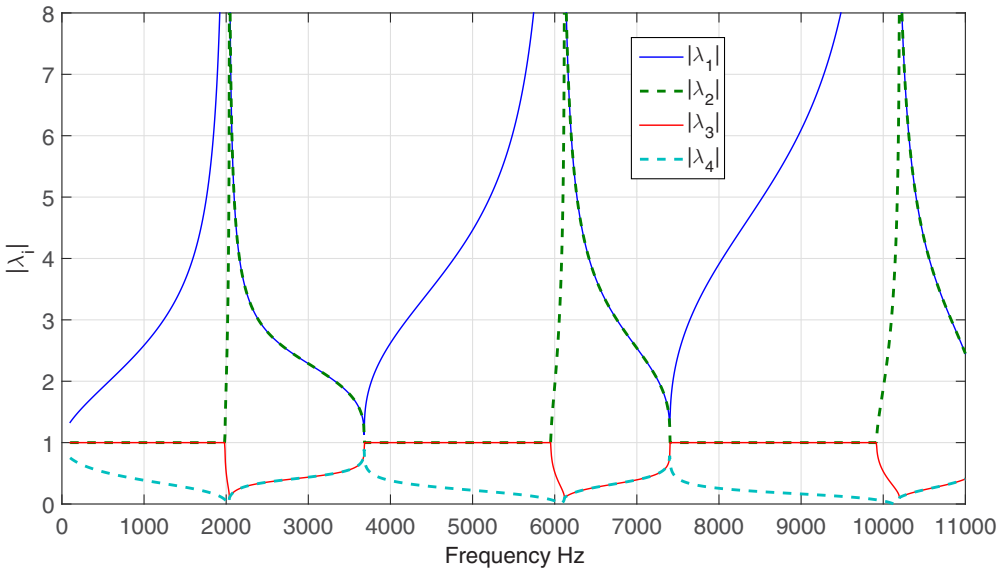

FIG. 8. (Color online) Exact results using the plate elastic parameters in Eq. (23). The absolute values of the four roots using MATLAB's roots function are plotted in different colors. The physical root for our problem is the red curve that displays the stop band and passband character.

where c_1 and d_1 are given by Eqs. (24) and (25). We have found that the four solutions of Eq. (23) (the roots) are simply given by

$$\lambda = \beta_\pm \pm (\beta_\pm^2 - 1)^{1/2}, \tag{A2}$$

which can be verified by substitution back into Eq. (23). This is apparently a general property of the solution of a fourth order polynomial equation when the coefficients of the λ^3 and λ terms are equal.

We consider two substitutions one for the root in the passband, and one for the root in the stop band. In the passband since the there is no attenuation let

$$\beta_p = \cos b, \tag{A3}$$

and in the stop band, now with attenuation,

$$\beta_s = \cosh(a \pm ib) = \cosh(a)\cos(b) \pm i \sinh(a)\sin(b). \tag{A4}$$

Introducing these into Eq. (A2), where a and b are real numbers, yields Eqs. (26) and (27) for λ_p (passband) and λ_s (stop band). We solve for a and b given $\cosh(a \pm ib) = \beta_s$ and for b given $\cos(b) = \beta_p$.

To obtain a and b we study Eq. (A1) and use a small order expansion in kL of Eqs. (24) and (25) that leads to an approximation for the square root term in Eq. (A1) good over a wide range of Θ up to $kL = 1.5$:

$$\left(2 + c_1^2 - d_1\right)^{1/2} \approx \left\{\left[\Xi + \frac{(kL)^4}{12}\right](\Xi + 12)\right\}^{1/2},$$

where we have defined $\Xi = \Theta(kL)^3/3$.

Given that $c_1 \approx \Xi + 2 + (kL)^4/12$ and defining $\tilde{\Xi} = \Xi + (kL)^4/12$ yields

$$\begin{aligned}\beta_\pm &= 1 + \frac{\tilde{\Xi}}{2} \pm \frac{1}{2}\sqrt{\tilde{\Xi}}\sqrt{\Xi + 12}, \\ &\approx 1 + \frac{\tilde{\Xi}}{2} \pm \frac{1}{2}\sqrt{\tilde{\Xi}}\sqrt{\tilde{\Xi} + 12},\end{aligned} \tag{A5}$$

where we approximated $\Xi + 12$ with $\tilde{\Xi} + 12$, valid within our restrictions on kL.

We cast $\tilde{\Xi}$ in terms of the attachment impedance using Eq. (4) to eliminate EI,

$$\begin{aligned}\tilde{\Xi} &\equiv \frac{(kL)^3}{12}\frac{\rho_b A_b c_b}{\rho A c_p}\tan(k_b L_b) + \frac{(kL)^4}{12} \\ &= \frac{(kL)^4}{12}\left[\frac{M_b}{M}\frac{\tan(k_b L_b)}{k_b L_b} + 1\right],\end{aligned} \tag{A6}$$

where $M = \rho A L$ is the mass of the rod segment, and M_b the total mass of the attached rod. Note the substitution $\tilde{\Xi} = \Xi + (kL)^4/12$ determines passband and stop band boundaries that occur when $\tilde{\Xi} = 0$ as we will make clear below.

In view of Fig. 8 only one of the roots in Eq. (A2), labeled λ_3, is the physical one we seek. In view of the two cases, Eqs. (A3) and (A4), we see that $\sqrt{\tilde{\Xi}}$ will be pivotal for determining the band nature. First, consider the case $\tilde{\Xi} > 0$. Equation (A5) shows that $\beta_\pm$ is then real, greater than unity for β_+, and less than unity for β_-. Considering Eq. (A2) the former leads to the two values of λ corresponding to λ_1 and λ_4 in Fig. 8, so we can rule out β_+ to represent our wave propagation solution. However, in the latter case we have in Eq. (A2), $(\beta_-^2 - 1)^{1/2} = i(1 - \beta_-^2)^{1/2}$, and Eq. (26) follows directly leading to an unattenuated wave traveling across the segment, that is, a passband.

Now consider the other case of when $\tilde{\Xi} < 0$ so that in Eq. (A5) $\sqrt{\tilde{\Xi}} = i\sqrt{|\tilde{\Xi}|}$. As long as $\tilde{\Xi} + 12 > 0$, violated only

extremely close to the antiresonances, then $\beta_\pm$ is a complex quantity and Eq. (A4) applies. This case defines the stop band where we choose the solution that decays across the segment. The equations in which we need to solve for a and b for the passband and stop band are, respectively,

$$b = \cos^{-1}\left(1 + \frac{\tilde{\Xi}}{2} - \frac{1}{2}\sqrt{\tilde{\Xi}}\sqrt{\tilde{\Xi}+12}\right), \tag{A7}$$

$$a + ib = \cosh^{-1}\left(1 - \frac{|\tilde{\Xi}|}{2} - \frac{i}{2}\sqrt{|\tilde{\Xi}|}\sqrt{12-|\tilde{\Xi}|}\right), \tag{A8}$$

that we rewrite as

$$b = \cos^{-1}(1-\epsilon), \tag{A9}$$

$$a + ib = \cosh^{-1}(1+\epsilon), \tag{A10}$$

given for Eq. (A7)

$$\epsilon \equiv \frac{1}{2}\sqrt{\tilde{\Xi}}\sqrt{\tilde{\Xi}+12} - \frac{1}{2}\tilde{\Xi}, \tag{A11}$$

and for Eq. (A8)

$$\epsilon \equiv -\frac{i}{2}\sqrt{|\tilde{\Xi}|}\sqrt{12-|\tilde{\Xi}|} - \frac{1}{2}|\tilde{\Xi}|, \tag{A12}$$

and use the small argument expansions

$$b = \cos^{-1}(1-\epsilon) \approx \sqrt{2\epsilon}\left(1 + \frac{\epsilon}{12} + \frac{3\epsilon^2}{160}\right), \tag{A13}$$

$$a + ib = \cosh^{-1}(1+\epsilon) \approx \sqrt{2\epsilon}\left(1 - \frac{\epsilon}{12} + \frac{3\epsilon^2}{160}\right). \tag{A14}$$

Using a series expansion in $\tilde{\Xi}$ of Eqs. (A11) and (A13) we obtain for the passband ($a = 0$ and $\tilde{\Xi} > 0$)

$$b \approx \sqrt{2}(3\tilde{\Xi})^{1/4}\left(1 + \frac{\tilde{\Xi}}{240} + \frac{\tilde{\Xi}^{3/2}}{168\sqrt{3}}\right). \tag{A15}$$

In the stop band ($\tilde{\Xi} < 0$) we obtain from Eqs. (A12) and (A14)

$$a = -(3|\tilde{\Xi}|)^{1/4}\left(1 - \frac{|\tilde{\Xi}|}{240} - \frac{|\tilde{\Xi}|^{3/2}}{168\sqrt{3}}\right), \tag{A16}$$

$$b = (3|\tilde{\Xi}|)^{1/4}\left(1 - \frac{|\tilde{\Xi}|}{240} + \frac{|\tilde{\Xi}|^{3/2}}{168\sqrt{3}}\right). \tag{A17}$$

We keep only the first term in these expansions since $\tilde{\Xi}$ is small over most of its range leading to Eqs. (28) and (29).

The equation for the beginning of the passband $\tilde{\Xi} = 0$, in view of Eq. (A6) is given by

$$\frac{M_b}{M}\frac{\tan(k_b L_b)}{k_b L_b} + 1 = 0. \tag{A18}$$

In other words, the condition $Z_b = 0$, the zero of the rod impedance, does *not* correspond exactly to the start of the the passband. Equation (A18) is a transcendental equation of the type $\tan(x) = -(M/M_b)x$.

[1] C. Kittel and P. McEuen, *Introduction to Solid State Physics*, Vol. 8 (Wiley, New York, 1976).

[2] E. Yablonovitch, Inhibited spontaneous emission in solid-state physics and electronics, Phys. Rev. Lett. **58**, 2059 (1987).

[3] J. D. Joannopoulos, S. G. Johnson, J. N. Winn, and R. D. Meade, *Photonic Crystals: Molding the Flow of Light* (Princeton University Press, Princeton, NJ, 2011).

[4] P. A. Deymier *et al.*, *Acoustic Metamaterials and Phononic Crystals*, Vol. 173 (Springer, New York, 2013).

[5] Z. Liu, X. Zhang, Y. Mao, YY Zhu, Z. Yang, C. T. Chan, and P. Sheng, Locally resonant sonic materials, Science **289**, 1734 (2000).

[6] J. B. Pendry, A. J._ Holden, D. J. Robbins, and W. J. Stewart, Magnetism from conductors and enhanced nonlinear phenomena, IEEE Trans. Microwave Theory Tech. **47**, 2075 (1999).

[7] N. Engheta and R. W. Ziolkowski, *Metamaterials: Physics and Engineering Explorations* (John Wiley & Sons, New York, 2006).

[8] Z. Liu, C. T. Chan, P. Sheng, A. L. Goertzen, and J. H. Page, Elastic wave scattering by periodic structures of spherical objects: Theory and experiment, Phys. Rev. B **62**, 2446 (2000).

[9] Y. Wu, Y. Lai, and Z.-Q. Zhang, Effective medium theory for elastic metamaterials in two dimensions, Phys. Rev. B **76**, 205313 (2007).

[10] F. Lemoult, M. Fink, and G. Lerosey, Acoustic resonators for far-field control of sound on a subwavelength scale, Phys. Rev. Lett. **107**, 064301 (2011).

[11] F. Lemoult, N. Kaina, M. Fink, and G. Lerosey, Wave propagation control at the deep subwavelength scale in metamaterials, Nature Phys. **9**, 55 (2013).

[12] N. Kaina, F. Lemoult, M. Fink, and G. Lerosey, Ultra small mode volume defect cavities in spatially ordered and disordered metamaterials, Appl. Phys. Lett. **102**, 144104 (2013).

[13] P. A. Belov, Y. Hao, and S. Sudhakaran, Subwavelength microwave imaging using an array of parallel conducting wires as a lens, Phys. Rev. B **73**, 033108 (2006).

[14] G. Lerosey, J. De Rosny, A. Tourin, and M. Fink, Focusing beyond the diffraction limit with far-field time reversal, Science **315**, 1120 (2007).

[15] F. Lemoult, M. Fink, and G. Lerosey, Revisiting the wire medium: An ideal resonant metalens, Waves Random Complex Media **21**, 591 (2011).

[16] J. Zhu, J. Christensen, J. Jung, L. Martin-Moreno, X. Yin, L. Fok, X. Zhang, and F. J. Garcia-Vidal, A. holey-structured metamaterial for acoustic deep-subwavelength imaging, Nature Phys. **7**, 52 (2011).

[17] D. Torrent and J. Sánchez-Dehesa, Effective parameters of clusters of cylinders embedded in a nonviscous fluid or gas, Phys. Rev. B **74**, 224305 (2006).

[18] M. Yang, G. Ma, Y. Wu, Z. Yang, and P. Sheng, Homogenization scheme for acoustic metamaterials, Phys. Rev. B **89**, 064309 (2014).

[19] M. Rupin, F. Lemoult, G. Lerosey, and P. Roux, Experimental demonstration of ordered and disordered multiresonant metamaterials for lamb waves, Phys. Rev. Lett. **112**, 234301 (2014).

[20] R. Graciá-Salgado, D. Torrent, and J. Sánchez-Dehesa, Quasi-two-dimensional acoustic metamaterials with negative bulk modulus, New J. Phys. **14**, 103052 (2012).

[21] C. Lagarrigue, JP Groby, and V. Tournat, Sustainable sonic crystal made of resonating bamboo rods, J. Acoust. Soc. Am. **133**, 247 (2013).

[22] A. Colombi, P. Roux, and M. Rupin, Sub-wavelength energy trapping of elastic waves in a metamaterial, J. Acoust. Soc. Am. **136**, EL192 (2014).

[23] K. E. Gilbert, A. propagator matrix method for periodically stratified media, J. Acoust. Soc. Am. **73**, 137 (1983).

[24] M. Schoenberg and P. N. Sen, Properties of a periodically stratified acoustic half-space and its relation to a biot fluid, J. Acoust. Soc. Am. **73**, 61 (1983).

[25] Y. Cheng, F. Yang, J. Y. Xu, and X. J. Liu, A. multilayer structured acoustic cloak with homogeneous isotropic materials, Appl. Phys. Lett. **92**, 151913 (2008).

[26] J. B. Pendry, D. Schurig, and D. R. Smith, Controlling electromagnetic fields, Science **312**, 1780 (2006).

[27] U. Leonhardt, Optical conformal mapping, Science **312**, 1777 (2006).